nature communications

Article

https://doi.org/10.1038/s41467-025-64638-x

Chiral metal cluster-mediated chirality transfer in light-harvesting nanoribbons for amplified circularly polarized luminescence

Received: 5 March 2025

Accepted: 23 September 2025

Published online: 31 October 2025

Check for updates

Tian-Li Gao[1], Jun-Ru Wang[1], Zhen Han[1], Jia-Yin Wang[1,2] ✉, Ying-Xue Yuan[1] ✉ & Shuang-Quan Zang[1] ✉

The construction of artificial light-harvesting systems (LHSs) with continuous chirality transfer is of great significance to deeply comprehend the hierarchical evolution in nature. Herein, the achiral C_3-symmetric benzene-1,3,5-tricarboxamide (BTA) molecule functions as donor of LHSs motifs, where subnanometer-scale metal clusters (*R*/*S*-Ag_6) are introduced as "Sergeants" to generate predominant handedness nanoribbons through chirality transfer. Importantly, these helical nanoribbons act as chirality and energy donors for the energy level-matching Ag_6-cluster acceptors, enabling the fabrication of chirality-controlled LHSs that achieve amplified circularly polarized luminescence (CPL) of Ag_6 clusters with a dissymmetry factor ($|g_{lum}|$) of 1×10^{-2}. Notably, the CPL signals of *R*/*S*-Ag_6 are further distinctly amplified with $|g_{lum}|$ reaching 6×10^{-2} through chirality-matching and synergistic effect of *R*/*S*-1-phenylethanol. Furthermore, *R*/*S*-Cu_6 clusters with near-infrared emission are employed as the second acceptor to construct relayed homochiral LHSs. Such LHSs program continuous chirality and energy transfers from BTA assemblies to Ag_6 and then to Ag_xCu_{6-x} alloy clusters, ultimately resulting in near-infrared CPL with $|g_{lum}|$ of 5×10^{-2}. This work provides valuable insight into the mechanisms of CPL transmission and amplification in cluster-driven chiral LHSs and opens potential application in chiroptical encryption.

Hierarchical assembly via bottom-up self-assembly orchestrates multiple molecular components into sophisticated architectures[1,2]. This approach plays a pivotal role in obtaining the structural complexity and functional diversity observed in biological systems[3–5]. It also provides an effective strategy for multiscale chirality transmission, spanning from molecular to macroscopic scales[6,7]. The formation of helical or twisted architectures through chiral molecular organization exemplifies this hierarchical propagation of chirality[8,9]. Introducing a small quantity of chiral molecules into a large quantity of achiral molecular matrix offers a simple and reliable approach for achieving the transmission of chirality, known as the "Sergeants and Soldiers" principle[10,11]. This process generates helical twisting forces that induce asymmetric superstructures at higher-dimensional scales, including supramolecular polymers, metal-organic frameworks, cages and liquid crystals[12–14]. Nevertheless, achieving continuous and handedness-controllable chirality transfer in these systems remains a challenge, necessitating the development of reliable assembly paradigms to reduce the dependence on high fidelity between chiral and achiral components. Among such chiral molecules, chiral ligand-protected coinage metal clusters (CMCs) exhibit diverse chiral origins, tunable luminescent properties, and versatile functionalities[15]. They are emerging as subnanoscale "Sergeants" with attractive potential for

[1]Henan Key Laboratory of Crystalline Molecular Functional Materials, College of Chemistry, Zhengzhou University, Zhengzhou, China. [2]Key Laboratory for Special Functional Materials of Ministry of Education, Henan University, Kaifeng, China. ✉e-mail: wangjiayin@henu.edu.cn; yuanyx@zzu.edu.cn; zangsqzg@zzu.edu.cn

transmitting chirality to achiral "Soldiers." However, studies on chiral CMCs act as "Sergeants" or chiral seeds with controllable chirality transfer have yet to be reported. Addressing the urgent need is essential to advance the functionality and broaden the applicability of CMC systems.

Artificial light-harvesting systems (LHSs) that utilize Förster resonance energy transfer (FRET) or triplet-triplet energy transfer (TTET) facilitate complex long-range excitation energy migration from energy donors to acceptors[16–20]. These LHSs have garnered great attention for their diverse applications in photodynamic/thermal therapy, bioapplication, white emitters, and photocatalysis[21–24]. Among them, LHSs containing chiral organizations are a desired motif for investigating continuous chirality transfer. In particular, the development of chiral LHSs constructed from helical structures has drawn increasing research attention[22,25–30], owing to their pivotal role in unraveling the mechanisms behind chiral information transmission and amplification. Accordingly, integrating chiral CMCs as "Sergeants" or chiral seeds into achiral supramolecular systems is crucial for the development of advanced artificial chiral LHSs. Such systems provide a unique platform for elucidating the mechanisms of continuous chirality transfer, energy transfer (ET), hierarchical evolution, and chiral amplification.

Circularly polarized luminescence (CPL) acts as a valuable monitor that reflects the difference of left-handed and right-handed circularly polarized light from the excited state[31–51]. CPL from chiral materials has high promise for application in optical display/detection[52–54], information encryption[55–57], and circularly polarized organic light-emitting diodes[58–61]. Moreover, CPL provides a powerful means to track chirality transfer and energy relay of luminescent materials in the excited states. Simultaneously, it can shed light on the hierarchical evolution of excited states of chirality. Atomically precise chiral CMCs constitute an emerging class of CPL-active materials[62–66], offering an ideal platform for investigating structure-property relationships at the molecular scale and elucidating the origin of chirality at the nanoscale. Nevertheless, these CMCs still face challenges associated with low dissymmetry factor (g_{lum}) and quantum yields (QY). Chiral CMCs exhibit strong luminescence and a broad chiral spectral range from blue to near-infrared light. They can serve as "Sergeants" or chiral seeds to generate controllable helical assemblies and extend the wavelength range of chiral emission. Moreover, through the required distance-based FRET mechanism, continuous chirality transfer and amplification of CPL can be realized between chiral luminescent CMCs and induced helical assemblies. This is particularly effective in chiral LHSs involving circularly polarized energy transfer (CPET) process, which can synchronously amplify both the g_{lum} and QY of CMCs assemblies.

Herein, the achiral benzene-1,3,5-tricarboxamide (BTA) molecule, featuring C_3-symmetry, was selected as the donor of the LHSs matrix due to its capability to form racemic supramolecular nanoribbons from a gel-like film. A small dose of chiral CMCs (*R*/*S*-Ag_6) was introduced as chiral seeds into the BTA assemblies to produce nanohelix structures through the "Sergeant and Soldier" principle. These nanohelixes exhibit bright blue emission and considerable CPL activity, which makes them suitable as a chirality and energy donor for the orange-light-emitting Ag_6 cluster acceptor. This enables the construction of chirality-controlled LHSs and realizes efficient ET and CPET. Intriguingly, the *R*/*S*-Ag_6 cluster was endowed with supramolecular chirality through helically oriented arrangement within the BTA/Ag_6 LHSs, resulting in amplified CPL with a $|g_{lum}|$ value of 0.01, attributed to efficient ET and CPET processes.

Notably, further amplification of the CPL signals was achieved with a $|g_{lum}|$ value of up to 0.06 upon incorporation of *R*/*S*-1-phenylethanol (*R*/*S*-phol), owing to high chirality matching and synergistic effect within homochiral BTA/phol/Ag_6 LHSs. To broaden the CPL spectral range, chiral *R*/*S*-Cu_6 clusters with near-infrared emission were introduced as the second acceptor into the homochiral BTA/phol/Ag_6 LHSs, forming metal cluster-relayed homochiral LHSs. Importantly, the Ag_6 clusters functioned as a relay baton, not only generating Ag_xCu_{6-x} alloy clusters with broader CPL emission but also facilitating programmed continuous chirality and ET from BTA assemblies to Ag_6 cluster and onward to Ag_xCu_{6-x} alloy clusters, leading to impressive near-infrared CPL with $|g_{lum}|$ of 0.05 and QY of 23% (Fig. 1). Capitalizing on the tunable luminescence and CPL performance of these LHSs, a three-dimensional (3D) barcode with high security level and convenient decryption functions was successfully fulfilled. This work paves the way for constructing chirality-controlled LHSs with high g_{lum} values and broad-spectrum CPL by leveraging chiral metal cluster-driven chirality transfer, and provides a practical example for CPL application in cluster-based information storage and encryption.

Results

Construction of helical nanoribbons via BTA assemblies with chiral Ag_6 and small chiral alcohols in a co-assembly system

Synthesis of BTA molecule: 4,4′,4″-((benzene-1,3,5-tricarbonyl)tris(azanediyl))tribenzoic acid was synthesized by the hydrolysis of triethyl 4,4′,4″-((benzene-1,3,5-tricarbonyl)tris(azanediyl))-tri-benzoate (compound 1, see Supplementary Figs. 1 and 2) and characterized by ^{1}H nuclear magnetic resonance (NMR) spectroscopy (Supplementary Fig. 3). BTA can self-assemble into nanoribbons structure via gel film state in a mixture of DMF and H_2O with a volume ratio of 6:4. These nanoribbons are delicate but not perfect because of the presence of almost equal amounts of *P*- and *M*-handed helixes (Figs. 1a and 2a), which results in chiroptical-active silent. Upon physical agitation or other stimulations, the BTA motif exhibits supramolecular chirality[67–71]. However, the helical direction of supramolecular assemblies obtained via the above-mentioned method is random, which leads to considerable confusion for BTA to have a wide range of applications in the chiroptical field. In this work, the BTA self-assembly event proceeded with a pronounced predominant chirality by adding a minor amount of atomically precise *S*- and *R*-Ag_6 clusters[62] as "Sergeant" or chiral seeds to afford *P*- and *M*-dominant nanoribbons, respectively (Figs. 1b and 2b, c). Vice versa, *R*- or *S*-Ag_6 was endowed with supramolecular chirality through embedding and orientation onto the BTA helix templates, as confirmed by transmission electron microscopy (TEM) observations (Fig. 2g, h and Supplementary Fig. 16).

Likewise, small chiral alcohols (*R*- and *S*-phol) act as chiral seeds that effectively induce predominant chirality in BTA assemblies. Specifically, BTA can self-assemble into recognizable left-handed helical nanoribbons by *R*-phol induction and right-handed helical nanoribbons by *S*-phol induction (Fig. 2d and Supplementary Fig. 4). Therefore, *R*-Ag_6 and *R*-phol, as well as *S*-Ag_6 and *S*-phol, exhibit homologous chirality in helical nanoribbon systems, which contribute to the investigation of their synergistic chirality. This perspective was confirmed by scanning electron microscopy (SEM) and TEM observations, which revealed that the BTA/*S*-phol/*S*-Ag_6 systems assembled into *P*-handed composite helixes with cluster-directed arrangement, while the BTA/*R*-phol/*R*-Ag_6 systems assembled into *M*-handed helixes with cluster-directed arrangement (Figs. 1c and 2g, h). Notably, the BTA/*R*- or *S*-phol assemblies possess the smaller helical pitches (348–390 nm) and wider helical diameters (140–178 nm), compared to those of BTA self-assemblies (pitch: 482 nm; diameter: 71 nm) (Fig. 2a, d and Supplementary Fig. 4). More intriguingly, the addition of *R*- or *S*-phol to BTA/Ag_6 homologous chirality systems, resulted in a reduction in helical pitches (from 436–464 to 341–346 nm) and an increase in helical diameters (from 103–109 to 121–131 nm) relative to the BTA/Ag_6 systems (Fig. 2b, c, e, f). These morphological size changes help to improve the chiroptical properties of metal cluster assemblies in excited states. Additionally, the homochiral BTA/phol/Ag_6 co-assemblies display higher homogeneity compared to BTA/phol

https://doi.org/10.1038/s41467-025-64638-x

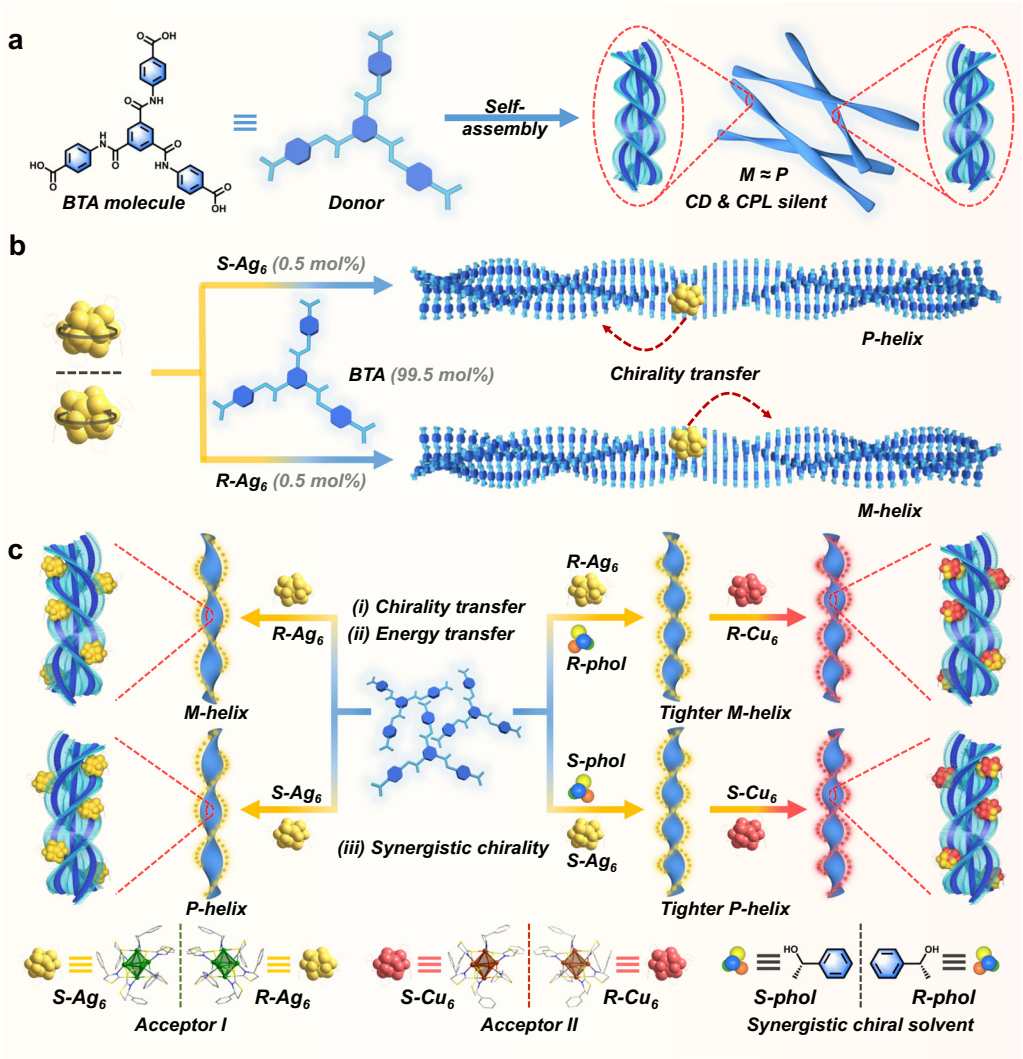

Fig. 1 | Schematic illustration of the processes: the self-assembly of BTA molecules into racemic nanoribbons, the metal cluster-triggered formation of helical nanoribbons, and the construction of chirality-controlled LHSs mediated by metal clusters. a Self-assembly of BTA molecules into racemic nanoribbons. **b** Introduction of small doses of *R*/*S*-Ag_6 clusters triggers the formation of helical nanoribbons through chirality transfer. **c** The helical nanoribbons serve as chiral/energy donors and assembly templates, co-assembling with *R*/*S*-Ag_6 clusters (first acceptor) and *R*/*S*-Cu_6 clusters (second acceptor), with a synergistic effect of *R*/*S*-phol to construct chirality-controlled LHSs exhibiting high g_{lum} and broad CPL spectral range.

co-assemblies, indicating that the introduction of *R*/*S*-Ag_6 clusters aids in regulating the dimensions of the co-assemblies.

Emission behaviors of chiral metal cluster-mediated LHSs

Under ambient conditions, BTA assemblies exhibit blue fluorescence with QY of 15.8%, while *R*/*S*-Ag_6 cluster assemblies from the film of DMF/H_2O (6:4, v/v) show bright orange emission with QYs of 11.6% and 10.8%, respectively (Supplementary Table 2). The emission spectra of BTA assemblies correspond well with the excitation spectra of Ag_6 clusters (Fig. 3a), facilitating an efficient ET process from the singlet (S) states of BTA assemblies to the S states of Ag_6 cluster (Fig. 3e). Therefore, with the increase in the ratios of *S*-Ag_6 clusters in the BTA gel-like assemblies, the emission intensity of *S*-Ag_6 at 573 nm progressively increased, accompanied by the red shift and the decrease in intensity of the BTA emission at 451 nm under the excitation of 330 nm (Supplementary Fig. 5). Concurrently, the emission color changed from blue to yellow-orange (Fig. 3c). These results indicate the successful construction of a mimetic LHSs based on the BTA/Ag_6 system. Intriguingly, the light-harvesting process was further validated in the BTA/*S*-phol/*S*-Ag_6 system through emission titration and decay experiments (Fig. 3b, d). The light-harvesting efficiency (Φ_{ET}) value reached 87.8% at 3% *S*-Ag_6 and 96.7% at 20% *S*-Ag_6 for the BTA/*S*-phol/*S*-Ag_6 system, while the Φ_{ET} value of BTA/*S*-Ag_6 system achieved 93.0% at 3% *S*-Ag_6 and 97.9% at 20% *S*-Ag_6, respectively. These results clearly demonstrate that the BTA/*S*-Ag_6 system exhibits consistently higher Φ_{ET} than the BTA/*S*-phol/*S*-Ag_6 system across different amounts of Ag_6 clusters (Fig. 3b, Supplementary Fig. 5 and Supplementary Table 1).

Furthermore, the BTA/*S*-phol/*S*-Ag_6 system showed a high QY of 31.2% at a 20% molar ratio of *S*-Ag_6, which has a 3-fold increase compared to the Ag_6 self-assembly (Supplementary Table 2). This enhancement implies that light loss can be avoided through an efficient ET process to improve the QY of the acceptor. Moreover, upon the addition of *S*-Ag_6 clusters, the emission lifetime of the BTA/*S*-phol/*S*-Ag_6 system decreased from $\tau = 2.23$ ns[67] to $\tau = 1.94$ ns with 0.1% addition, and further to $\tau = 1.60$ ns with 20% addition, measured at 451 nm (Fig. 3d and Supplementary Table 3). These results confirm the occurrence of an efficient light-harvesting process in the BTA/*S*-phol/*S*-Ag_6 systems.

Chiral hierarchical assembly mechanism of supramolecular co-assembly systems

The fascinating chirality of BTA assemblies triggered by *R*/*S*-Ag_6 clusters and *R*/*S*-phol prompted us to further investigate the hierarchical

https://doi.org/10.1038/s41467-025-64638-x

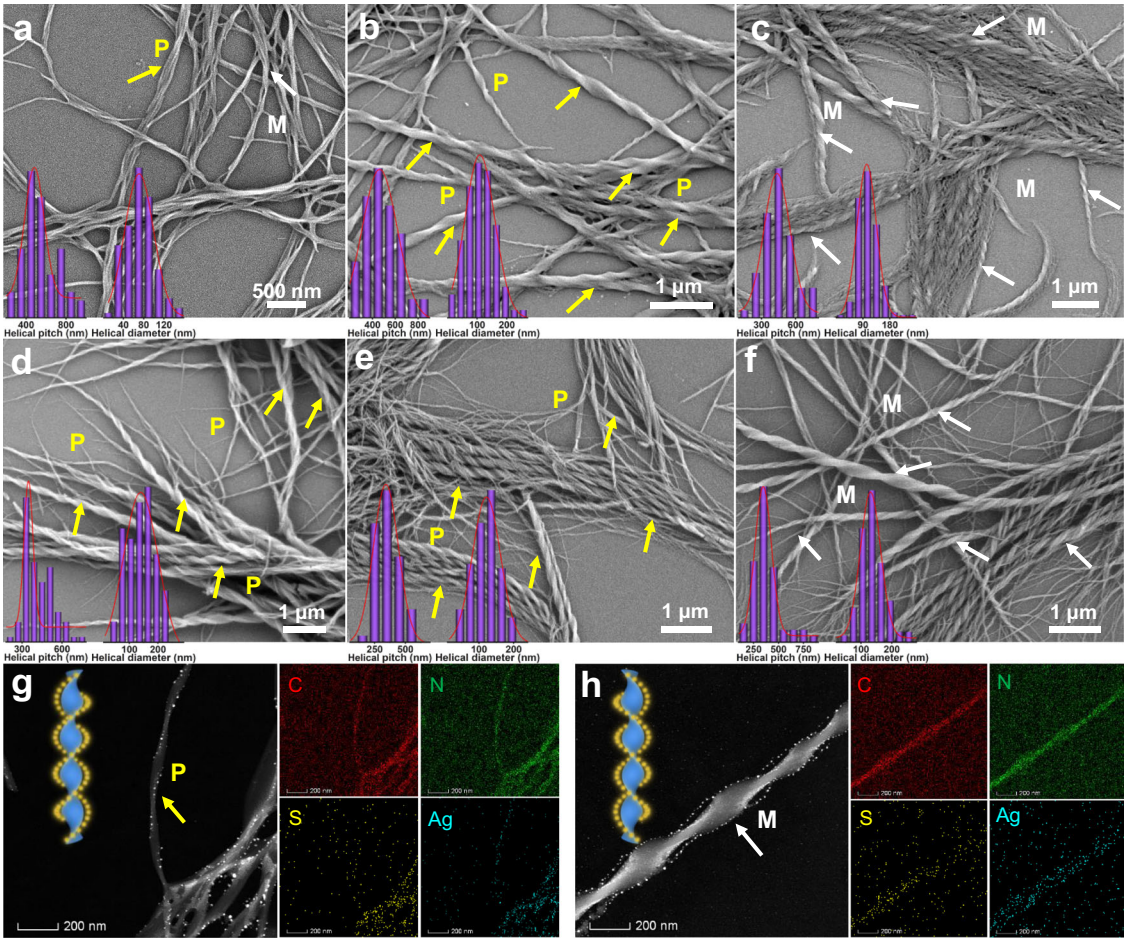

Fig. 2 | The formation of helical nanoribbons triggered by chiral seeds of *R*- or *S*-Ag_6, and the hierarchical evolution of helical nanoribbons with the synergistic effect of *R*- or *S*-phol. a SEM images of achiral BTA self-assemblies. **b** SEM images of BTA/*S*-Ag_6 co-assemblies. BTA/*S*-Ag_6 = 100:3. **c** SEM images of BTA/*R*-Ag_6 co-assemblies. BTA/*R*-Ag_6 = 100:3. **d** SEM images of BTA/*S*-phol assemblies. BTA/*S*-phol = 100:7. **e** SEM images of BTA/*S*-phol/*S*-Ag_6 co-assemblies. BTA/*S*-phol/*S*-Ag_6 = 100:7:3. **f** SEM images of BTA/*R*-phol/*R*-Ag_6 co-assemblies. BTA/*R*-phol/*R*-Ag_6 = 100:7:3. **g** HAADF images and elemental mappings of BTA/*S*-phol/*S*-Ag_6 co-assemblies. BTA/*S*-phol/*S*-Ag_6 = 100:7:10. **h** HAADF images and elemental mappings of BTA/*R*-phol/*R*-Ag_6 co-assemblies. BTA/*R*-phol/*R*-Ag_6 = 100:7:10. Insert of (**a**–**f**): Histograms of helical pitch (average values: 482, 464, 436, 348, 341, 346 nm) and helical diameter (average values: 71, 109, 103, 140, 121, 131 nm).

assembly mechanism of composite helical nanostructures. BTA molecules exhibit strong intermolecular hydrogen bonding, C−H•••π interactions, and π•••π hole interactions (Supplementary Fig. 6), enabling their assembly into nanoribbon structure in DMF/H_2O system (6:4, v/v) (Fig. 2a). In contrast to the almost no circular dichroism (CD) signals from BTA self-assembled nanoribbons (Supplementary Fig. 7a), the introduction of tiny amounts of chiral seeds *R*-/*S*-Ag_6 or *R*-/*S*-phol displayed a strong mirror-image Cotton effect split peak at 320 nm in the CD spectra of BTA nanoribbons (Supplementary Figs. 8a, 10e and 13e), exhibiting distinct supramolecular helical chirality. Specifically, increasing the amount of chiral Ag_6 clusters by only 0.5% in BTA assemblies facilely generated predominant chirality in BTA nanoribbons (Fig. 1b and Supplementary Figs. 10a and 25). The CD spectra of BTA/Ag_6 co-assemblies exhibited positive CD signals with *R*-Ag_6 and a negative Cotton effect with *S*-Ag_6 (Supplementary Fig. 10a, c, e). Additionally, left-handed helixes of co-assemblies were obtained with *R*-Ag_6, and right-handed helixes of co-assemblies were formed with *S*-Ag_6, which are consistent with the morphological changes characterized in SEM images (Fig. 2b, c). As the amount of Ag_6 cluster increased from 0.5% to 20%, the dissymmetry factors of CD (g_{abs}) of the BTA/Ag_6 assemblies reached ~±5.0–7.0 × 10^{-3} (Supplementary Fig. 10 and Supplementary Table 4). In comparison, when *R*- and *S*-ligands were used as chiral seeds, the CD spectra of BTA assemblies were investigated. The TEM images reveal that BTA assemblies formed a *P* and *M* helix by embedding assembly with *S* and *R*-ligand, respectively (Supplementary Fig. 11), but the weaker CD signals were obtained compared with those when *S*-Ag_6 and *R*-Ag_6 were used as chiral seeds in BTA assemblies (Supplementary Fig. 12 and Supplementary Table 5). These results indicate that the exceptional efficacy of the chiral Ag_6 clusters as chiral seeds. The possible reasons might be attributed to the formation of helical arrangement of chiral ligands on the Ag_6 cluster shell (Supplementary Fig. 38), facilitating the generation of a homochirality field of the helical LHSs. More interestingly, BTA assemblies incorporating *R*-phol exhibited positive Cotton effect, while those with *S*-phol exhibited negative Cotton effect (Supplementary Fig. 8), which are consistent with the helical direction of the morphologies observed in SEM images (Fig. 2d and Supplementary Fig. 4). Moreover, the homochiral *R*-phol and *R*-Ag_6 clusters (*S*-phol and *S*-Ag_6 clusters) as chiral seeds not only generated elegant helical morphology of BTA assemblies, but also synergistically enhanced the chiroptical signals of BTA/Ag_6 systems (Fig. 4g). Expectedly, the introduction of *R*/*S*-phol can aid in attaining larger g_{abs} (~±1.4–2.4 × 10^{-2}) for BTA/Ag_6 co-assemblies, which is mainly attributed to the smaller and tighter pitches of the nanohelixes after the addition of *R*- or *S*-phol (Supplementary Fig. 13 and Supplementary Table 6). Interestingly, the ^{1}H NMR spectroscopy was performed to investigate the C−H···π

https://doi.org/10.1038/s41467-025-64638-x

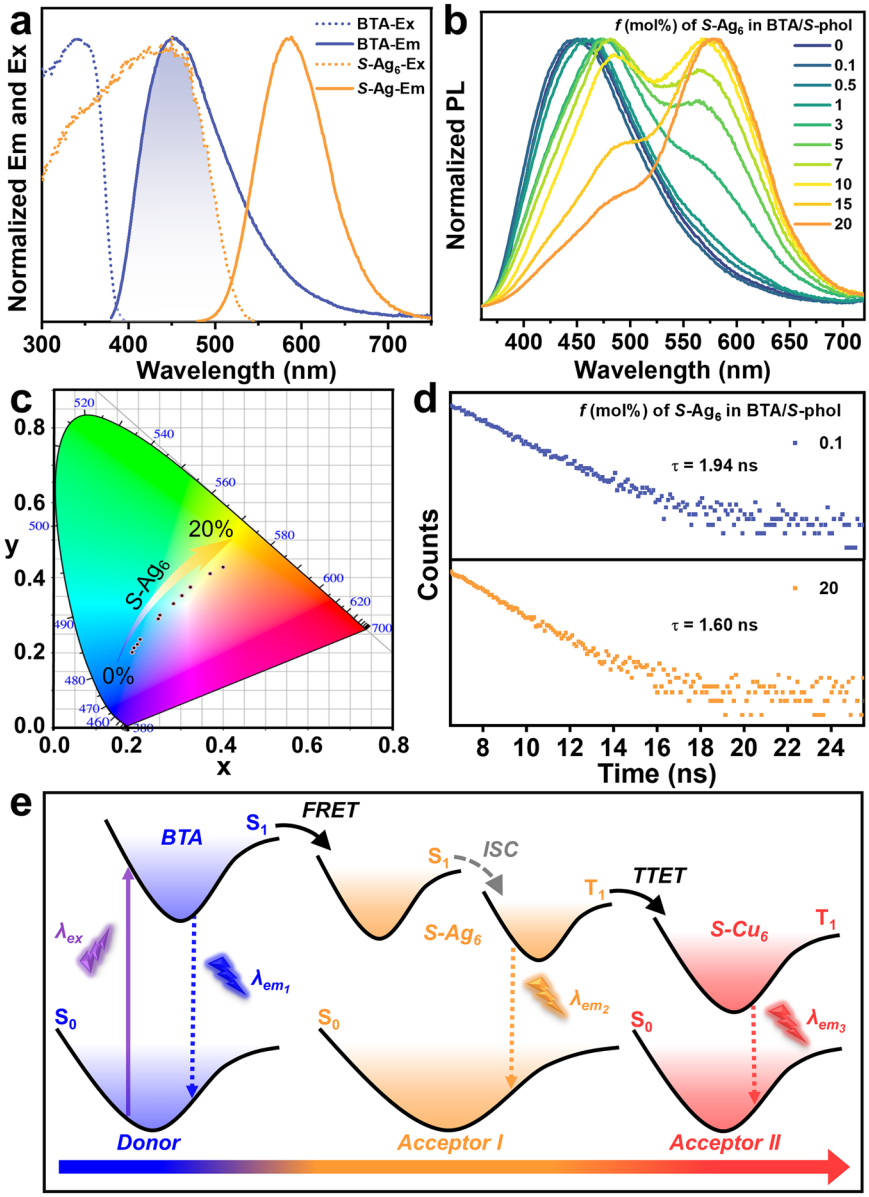

Fig. 3 | Energy transfer in homochiral BTA/phol/Ag_6 LHSs. a Normalized excitation and emission spectra of BTA self-assemblies, and normalized excitation and emission spectra of Ag_6 clusters. **b** Normalized PL spectra of BTA/*S*-phol (100:7) with different molar ratios of *S*-Ag_6 (0%–20%), λ_{ex} = 330 nm. **c** CIE chromaticity coordinates changes of (**b**). **d** Emission decay profiles of BTA/*S*-phol (100:7) with 0.1% and 20% molar ratios of *S*-Ag_6 at 451 nm, λ_{ex} = 330 nm. **e** Illustration of the FRET and TTET processes in the BTA/*S*-phol/*S*-Ag_6/*S*-Cu_6 system.

interaction between BTA and Ag_6/phol. These observations confirm that chirality transfer from *R*/*S*-Ag_6 to BTA occurs predominantly through C–H···π interactions, whereas *R*/*S*-phol induces a stronger chiral response in BTA via both C–H···π interaction and hydrogen bonding (Supplementary Fig. 14).

In both the BTA/Ag_6 and BTA/phol/Ag_6 systems, no discernible CD signals originating from Ag_6 clusters were observed at longer wavelengths, even when the concentration of Ag_6 clusters reached up to 20% (Supplementary Figs. 9 and 10). This is attributed to the macroscopic ordering and pronounced structural anisotropy of BTA-based supramolecular helices, resulting in considerable light scattering during CD measurement, which covers up the CD contribution from the Ag_6 clusters. To exclude the effect of self-scattering from the BTA-based assemblies in supramolecular-induced chirality, fluorescence-detected circular dichroism (FDCD) was further employed. As shown in the FDCD spectra in Fig. 4a–c, the BTA/Ag_6 and BTA/phol/Ag_6 assemblies exhibit clearly characteristic chiral signals of Ag_6 clusters in the range of 350–500 nm, while the BTA/phol assemblies display mirror-symmetric characteristic signals of BTA at 300–380 nm. In addition, the BTA self-assemblies have almost no FDCD signals (Supplementary Fig. 7b). These FDCD results indicated that Ag_6 clusters acquire supramolecular chirality in the excited state within the BTA/Ag_6 and BTA/phol/Ag_6 assemblies.

To better comprehend the assembly mechanism of the homochiral BTA/phol/Ag_6 systems, the morphological changes in co-assemblies containing different molar ratios of Ag_6 clusters were investigated by SEM and TEM. The results indicate that when the molar ratio of Ag_6 clusters is below 3%, the homochiral Ag_6 clusters bind uniformly to the BTA helical nanoribbons. Additionally, when the molar ratio exceeds 10%, the excess Ag_6 clusters get aggregated into nanoparticles that align along the nanohelixes, forming cluster-based composite nanohelixes (Supplementary Figs. 15 and 16). This observation was confirmed by TEM elemental mappings, which clearly reveal the formation of the helically arranged nanoparticles through

https://doi.org/10.1038/s41467-025-64638-x

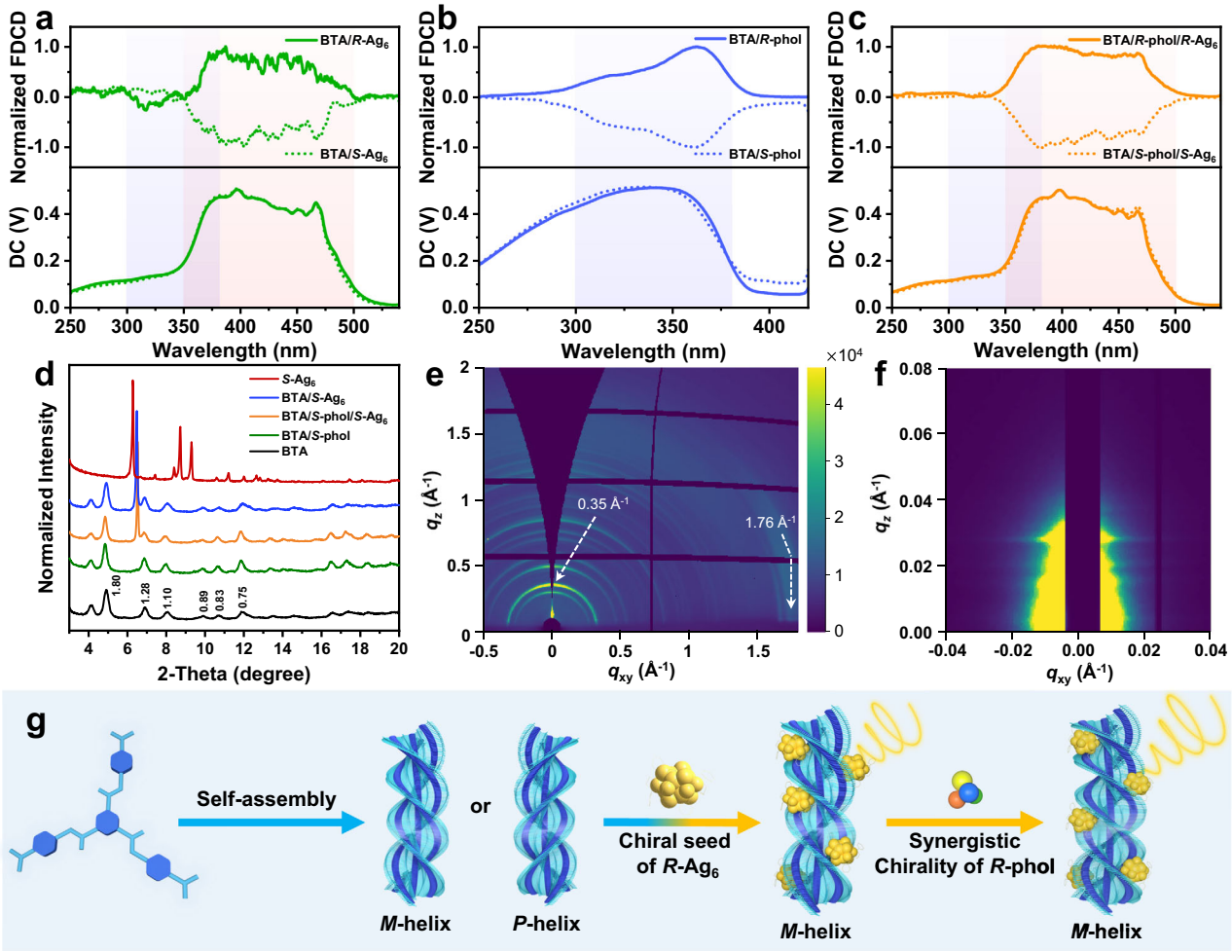

Fig. 4 | FDCD, PXRD, GIWAXS spectra, and mechanism diagram of the co-assembled system. a Normalized FDCD spectra of BTA/*R*- or *S*-Ag_6 (molar ratio 100:20). **b** Normalized FDCD spectra of BTA/*R*- or *S*-phol (100:7). **c** Normalized FDCD spectra of BTA/*R*-phol/*R*-Ag_6 and BTA/*S*-phol/*S*-Ag_6 (100:7:20). **d** PXRD patterns of BTA, BTA/*S*-phol (100:7), BTA/*S*-phol/*S*-Ag_6 (100:7:0.5), BTA/*S*-Ag_6 (100:0.5), and *S*-Ag_6, d-spacing (unit: nm) corresponding to diffraction peaks. **e** GIWAXS pattern of BTA self-assemblies. **f** GISAXS pattern of BTA self-assemblies. **g** Illustration of the self-assembly process of achiral BTA molecule into homochiral helix mediated by chiral seed of *R*-Ag_6 via chirality transfer, with amplified CPL through the synergistic chirality of *R*-phol. Note: The blue shadings in (**a**–**c**) indicate the signal region for BTA, and the orange shadings indicate the signal region for *R*/*S*-Ag_6.

the aggregation of Ag_6 clusters (Fig. 2g, h). Furthermore, SEM images of Ag_6 clusters obtained under the same conditions as the control experiment exhibit the presence of large spherical aggregates (Supplementary Fig. 17).

For more detailed elucidation of the assembly mechanism of BTA assemblies with Ag_6 cluster, the ultraviolet-visible (UV-Vis) spectroscopy, electrospray ionization-mass spectrometry (ESI-MS), Fourier transform infrared (FT-IR) spectroscopy, and powder X-ray diffraction (PXRD) analyses of these co-assemblies were conducted. The UV-Vis spectra demonstrated that when the molar ratio of Ag_6 clusters exceeded 0.5%, both BTA/Ag_6 and BTA/phol/Ag_6 co-assemblies exhibited distinct absorption bands of Ag_6 at 380–500 nm region (Supplementary Fig. 18). In combination with the results of high-resolution mass spectrometry (HRMS) of disassembled Ag_6 clusters was consistent with the initial Ag_6 clusters, implying that high stability of Ag_6 clusters in the co-assembly systems (Supplementary Fig. 19). FT-IR spectra exhibit a vibration band at 1656.3 cm^{-1}, assigned to the carboxyl group, and the peaks at 1596.6 and 1526.5 cm^{-1}, corresponding to the characteristic peaks of amide I and amide II bands, respectively. The shift of the vibration bands to lower wavenumbers suggests the formation of intermolecular hydrogen bonds (Supplementary Fig. 20). Moreover, the S-C vibration bands of Ag_6 clusters were clearly observed at 1032.1 cm^{-1} and 976.5 cm^{-1} in the cluster-based LHSs (Supplementary Fig. 20i). With the increase in the content of Ag_6 clusters, the S-C vibration bands gradually enhanced while those of BTA assemblies remain intact, indicating successful integration of Ag_6 clusters into the BTA assemblies. The PXRD pattern of BTA assemblies exhibited a series of regular diffraction peaks at 4.90, 6.91, 8.05, 9.90, 10.67, and 11.84° corresponding to d-spacings of 1.80, 1.28, 1.10, 0.89, 0.83, and 0.75 nm, respectively. These values are in line with a ratio of 1: 1/√2: 1/√3: 1/√4: 1/√5: 1/√6, which indicates the formation of a lamellar structure (Fig. 4d). This result is consistent with the hierarchical assembly of BTA observed in the TEM image (Supplementary Fig. 21). Furthermore, self-assembly mechanism of BTA was investigated by grazing-incidence wide-angle X-ray scattering (GIWAXS), the lamella stacking peak at 0.35 $Å^{-1}$ appeared out-of-plane, while the π•••π stacking peak at 1.76 $Å^{-1}$ was in-plane[72] (Fig. 4e and Supplementary Fig. 22a). Correspondingly, the coherence lengths are $D_{out\text{-}of\text{-}plane}$ = 19.8 nm and $D_{in\text{-}plane}$ = 4.1 nm, calculated using the Scherrer equation[73,74] ($D = 2\pi K/\Delta q$, K ~ 0.9, Supplementary Fig. 23a). These results indicate that the vertical expansion of BTA helical nanoribbons occurs primarily along the lamellar stacking direction, whereas their elongation proceeds along the π•••π stacking direction. This anisotropy aligns with the preferential growth mechanism

observed in BTA nanoribbons. Additionally, the grazing-incidence small-angle X-ray scattering (GISAXS) showed a distinct out-of-plane Bragg peak (Fig. 4f). The out-of-plane 1D GISAXS profile of BTA nanoribbons exhibits a peak at $q_z = 0.029$ Å^{-1} (d-spacing = 21.7 nm), confirming long-range order between nanoribbons along the out-of-plane direction. This well-defined periodicity suggests that strong packing interaction makes for the hierarchical assembly[72,75] (Supplementary Fig. 22b). The PXRD pattern of BTA/*S*-phol co-assemblies was slightly shifted relative to BTA self-assemblies, indicating incorporation of *S*-phol into the nanoribbons without disrupting the assembled structure of BTA nanoribbons. Similarly, the addition of Ag_6 clusters did not disturb the peak pattern of the BTA assemblies but caused a slight shift (Fig. 4d). This implies that some Ag_6 clusters were embedded within the BTA assemblies, which promotes efficient ET and chirality transfer from BTA to the Ag_6 clusters. Notably, the addition of *S*-Ag_6 clusters led to a new diffraction peak at 6.48° (d = 1.36 nm) in the PXRD pattern of BTA or BTA/*S*-phol assembly films, suggesting that a portion of Ag_6 clusters was deposited on the surface of the BTA helical nanoribbons. This peak arose from the angular shift of the diffraction peak located at 6.29° (d = 1.41 nm), which corresponds to the characteristic (001) crystal plane in *S*-Ag_6. This obvious shift ($\Delta d = -0.05$ nm) is primarily attributed to lattice compression induced by the ordered arrangement of Ag_6 clusters along the BTA helical nanoribbons (Supplementary Fig. 23b). Moreover, no new diffraction peaks appeared with the increase in the molar ratio of Ag_6, indicating that the *S*-Ag_6 clusters adopted a preferred orientation during the co-assembly process (Fig. 4d and Supplementary Fig. 24). Even at the molar ratio of Ag_6 up to 20%, the diffraction peaks of BTA assemblies remain intact, implying that BTA/Ag_6 and BTA/phol/Ag_6 co-assemblies retain stable and well-ordered helical structures (Supplementary Fig. 24e, i). Combined with the TEM analysis, these results reveal that a fraction of the Ag_6 clusters were embedded within the BTA helical nanoribbons, while the excess Ag_6 clusters were distributed on the surface and even aligned along the helical direction of the nanoribbons.

Synergistic amplification of circularly polarized luminescence

Similar to the CD and FDCD spectra, a small amount of Ag_6 (0.5%) was sufficient to trigger the CPL signal of BTA assemblies. The BTA/*R*-Ag_6 co-assemblies showed a left-handed CPL signal at 480 nm (g_{lum} = +0.0132), while the BTA/*S*-Ag_6 co-assemblies exhibited a right-handed CPL signal at 480 nm (g_{lum} = −0.0139) under 330 nm excitation (Fig. 5a and Supplementary Table 9). The handedness of the CPL signals was consistent with the helical direction of morphologies of BTA/Ag_6 co-assemblies (Fig. 2b, c and Supplementary Fig. 25). For comparative analysis, CPL spectra of BTA/*R*-ligand (or BTA/*S*-ligand) co-assemblies with *R*-ligand or *S*-ligand (0.5%-20%) were studied. The weak and single CPL signal was obtained, and the g_{lum} value was only ~ $\pm 10^{-3}$ under the same conditions (Supplementary Fig. 26). This result underscores that the Ag_6 cluster with the helical arrangements of chiral peripheral ligands plays an irreplaceable role in inducing helical chirality of BTA assemblies and generates strong CPL. To further verify the stability of *R*-Ag_6 and *S*-Ag_6 clusters as chiral seeds capable of inducing predominant helical chirality in BTA assemblies, the CPL spectra of 10 batches of BTA/Ag_6 (100:0.5) assemblies were measured under 330 nm excitation (Supplementary Fig. 27 and Supplementary Table 7). This result manifests that chiral Ag_6 clusters as chiral seeds generate predominant helical chirality with high stability in the chiral orientation and large g_{lum} value, highlighting their potential as chiral seeds for programmable chirality transfer in supramolecular LHSs.

The solid-state emission spectra of Ag_6 clusters at different excitation wavelengths showed that the emission intensity under 330 nm excitation was weaker than that under 400 nm excitation (Supplementary Fig. 28). Furthermore, excitation spectra displayed that BTA could not be effectively excited under 400 nm excitation (Fig. 3a).

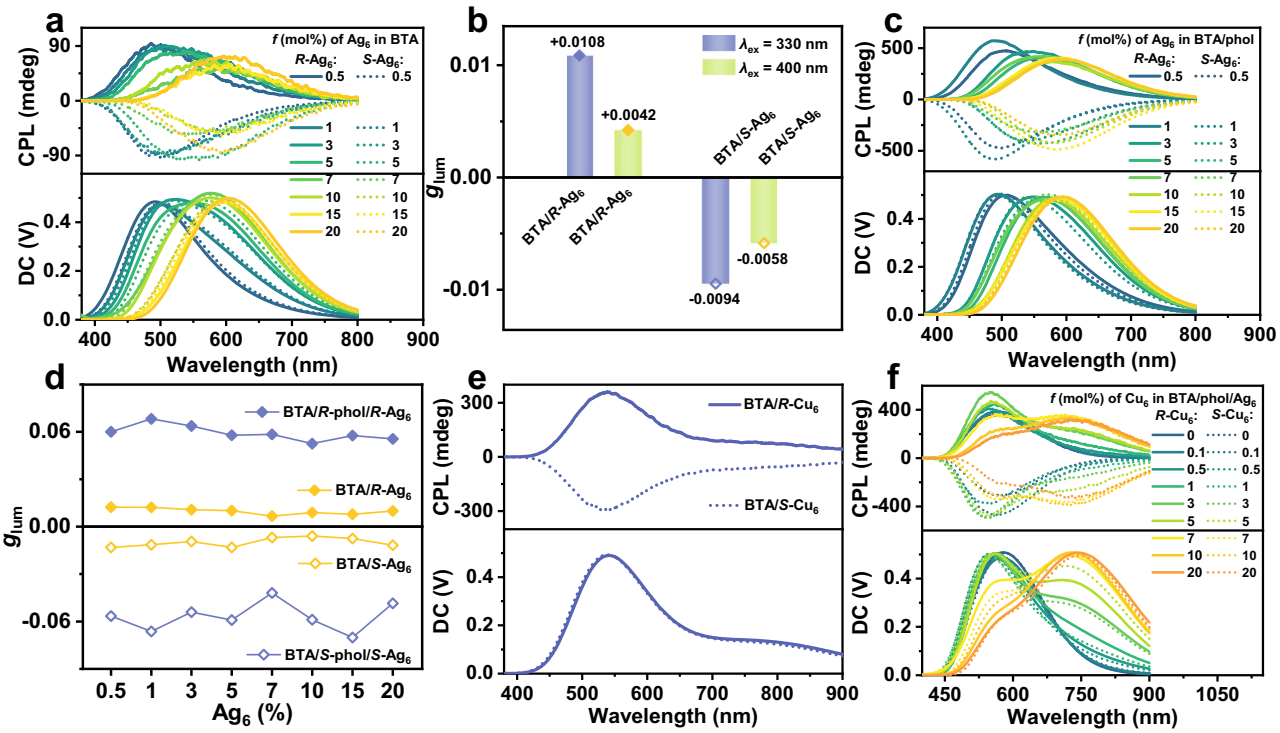

Fig. 5 | CPL spectra of the BTA/Ag_6-based co-assembled system. a CPL spectra of BTA with different molar ratios of Ag_6 (0.5%–20%), λ_{ex} = 330 nm. **b** CPL g_{lum} of BTA/Ag_6 co-assemblies (molar ratio 100:3) at 600 nm with different excitation wavelengths. **c** CPL spectra of BTA/phol (100:7, v/v) with different molar ratios of Ag_6 (0.5%–20%), λ_{ex} = 330 nm. **d** CPL g_{lum} values at 600 nm of BTA/Ag_6 co-assemblies (molar ratio 100:0.5–100:20) and BTA/phol/Ag_6 co-assemblies (molar ratio 100:7:0.5–100:7:20), λ_{ex} = 330 nm. **e** CPL spectra of BTA/Cu_6 co-assemblies (molar ratio 100:20), λ_{ex} = 330 nm. **f** CPL spectra of BTA/phol/Ag_6 (molar ratio 100:7:10) with different molar ratios of Cu_6 (0.1%–20%), λ_{ex} = 330 nm.

Therefore, the comparative CPL spectra were conducted under both excitation conditions. When the molar ratio of Ag_6 was increased to 1%, the g_{lum} value of BTA/*R*-Ag_6 co-assemblies was +0.0081, and that of BTA/*S*-Ag_6 co-assemblies was −0.0079 under 400 nm excitation. However, the g_{lum} value of *R*-Ag_6 nanospheres was −0.0014, and that of *S*-Ag_6 nanospheres was +0.0017, which are in the opposite direction of the CPL signals of the BTA/Ag_6 co-assemblies (Supplementary Fig. 29).

These results suggest that *R*-Ag_6 or *S*-Ag_6 can not only produce predominant helical chirality in BTA assemblies, but also amplify the g_{lum} of Ag_6 cluster via imparted supramolecular chirality and ET process. Intriguingly, as the molar ratio of Ag_6 increased, the CPL emission peak of the BTA/Ag_6 co-assemblies gradually bathochromic-shifted under 330 nm excitation, which implies the occurrence of the CPET process. As expected, when the molar ratio of Ag_6 reached 3%, an obvious CPL signal of Ag_6 clusters appeared. Under 330 nm excitation, the g_{lum} value of the BTA/*R*-Ag_6 co-assemblies was found to be +0.0108 and that of BTA/*S*-Ag_6 was −0.0094 at 600 nm, which were 2.6-fold and 1.6-fold larger than for those excited at 400 nm (for BTA/*R*-Ag_6, the g_{lum} was +0.0042; for BTA/*S*-Ag_6, the g_{lum} was −0.0058), respectively (Fig. 5b and Supplementary Fig. 30). Subsequently, as Ag_6 clusters continue to increase (5%–20%), CPET process was detected by CPL spectroscopy (Fig. 5a, Supplementary Fig. 32, and Supplementary Tables 9 and 10). These data clearly indicate the realization of the CPET handoff and CPL amplification from the BTA assemblies to *R*-Ag_6 (*S*-Ag_6) clusters.

To further enhance the g_{lum} of the Ag_6 clusters, *R*/*S*-phol with strong chirality-inducing ability was introduced to amplify the chiroptical signals of the co-assemblies containing homochiral Ag_6 clusters via a synergistic effect. Initially, the chirality induction behavior of BTA assemblies with *R*-phol or *S*-phol in the excited state was investigated. Comparative analysis revealed that chiral seeds of Ag_6 clusters can induce both blue light CPL of BTA assemblies and yellow light CPL of the Ag_6 clusters themselves (Fig. 5a); however, *R*-phol and *S*-phol only induce blue light CPL of BTA assemblies. Nevertheless, they can obtain stronger CPL signals at 472 nm under 330 nm excitation (Supplementary Fig. 31a). By increasing the doses of *R*-phol or *S*-phol, the g_{lum} value of BTA assemblies reached the maximum at a loading of 7%, with values of +0.00622 and −0.0598 at 472 nm, respectively (Supplementary Fig. 31 and Supplementary Table 8). Therefore, 7% doses of *R*-phol or *S*-phol were selected to incorporate into the homochiral BTA/Ag_6 co-assemblies to enhance the g_{lum} value of Ag_6 clusters in the following experiment. When the molar ratios of *R*-Ag_6 and *S*-Ag_6 were 3%, the g_{lum} values of Ag_6 in the BTA/phol/Ag_6 co-assemblies reached +0.0637 and −0.0541, respectively, which is 6-fold larger than those of the BTA/Ag_6 system and 30-fold larger than those of Ag_6 self-assemblies under 330 nm excitation (where g_{lum} = +0.0108 for BTA/*R*-Ag_6, −0.0094 for BTA/*S*-Ag_6, −0.0021 for *R*-Ag_6 and +0.0021 for *S*-Ag_6) (Fig. 5a, c, d and Supplementary Fig. 33 and Supplementary Tables 9 and 11). However, the g_{lum} values of the BTA/phol/Ag_6 co-assemblies under 330 nm excitation were not obviously enhanced compared to those under 400 nm excitation (g_{lum} = +0.0648 for BTA/*R*-phol/*R*-Ag_6, and −0.0535 for BTA/*S*-phol/*S*-Ag_6). This can be attributed to the strong chiral induction from *R*/*S*-phol, which likely masks the CPET process (Fig. 5c, Supplementary Fig. 34 and Supplementary Tables 11 and 12). As a control experiment, CPL spectra of *R*-phol/*R*-Ag_6 and *S*-phol/*S*-Ag_6 mixtures were investigated, showing g_{lum} values of −0.0021 and +0.0020, respectively (Supplementary Fig. 35), which were not obviously amplified compared to Ag_6 self-assemblies. These data demonstrate that using (*R*-Ag_6 and *R*-phol) or (*S*-Ag_6 and *S*-phol) as chiral seeds promotes stronger helical chirality in BTA assemblies and synergistically increases the g_{lum} value of the co-assembled systems. Combined with the variations in helical diameter and pitch observed across these systems, we propose a potential correlation between helical dimensions and CPL signals: smaller helical pitches and larger helical diameters may enlarge the $|g_{lum}|$ value of systems.

Furthermore, rotational experiments were performed on the chiral BTA/phol, BTA/Ag_6, and BTA/phol/Ag_6 systems to rule out contributions from linear polarization; the results demonstrated negligible interference[28,76,77] (Supplementary Fig. 36).

To extend the outputs of CPL spectrum, chiral Cu_6 clusters were selected because they emit near-infrared phosphorescence with broad absorption in the solid state, and their configuration is similar to that of chiral Ag_6 clusters (Supplementary Figs. 37 and 38). *R*- or *S*-Cu_6 was synthesized according to a similar literature method[65]. Fortunately, their single crystal suitable for X-ray diffraction analysis was obtained by slow evaporation of a DMF/acetonitrile mixture at room temperature over several days. Their crystal structure (CCDC 2394282 for *R*-Cu_6 and 2394819 for *S*-Cu_6) manifests that the *R*- or *S*-ligand is helically arranged around the metal core (Supplementary Fig. 38c, d), which favors them as chiral seeds to generate helical superstructure. Similar to Ag_6 clusters, Cu_6 clusters as chiral seeds can also trigger helical chirality in BTA assemblies, but cannot be endowed with supramolecular chirality. The FDCD spectra of BTA/Cu_6 assemblies exhibited only the characteristic signals of BTA (Supplementary Figs. 39 and 40), and the CPL signal of Cu_6 clusters are still weak even at a molar ratio of 20% of Cu_6 clusters (Fig. 5e). Fortunately, the emission spectrum of *S*-Ag_6 assemblies overlaps well with the excitation spectrum of *S*-Cu_6 assemblies (Supplementary Fig. 41), facilitating the ET process from triplet (T) states of Ag_6 clusters to T states of Cu_6 clusters (Fig. 3e). Subsequently, the addition of 10% Ag_6 clusters as relay baton to the homochiral BTA/Cu_6 co-assemblies resulted in a bright red CPL spectral output (Supplementary Fig. 42). This result indicates the occurrence of a possible TTET process from the homochiral Ag_6 to Cu_6 clusters, which was confirmed by emission spectra and lifetime decay experiments (Supplementary Figs. 43–45). As the doses of Cu_6 clusters increased under 330 nm excitation, the emission intensity at 573 nm gradually weakened and eventually disappeared, while the emission intensity at 750 nm gradually increased. Concurrently, the emission intensity at 451 nm first increased and then decreased once the Cu_6 cluster content reached 5% (Supplementary Figs. 43a and 44a). Moreover, the emission intensity at 573 nm gradually disappeared, and that at 750 nm intensified under 400 nm excitation (Supplementary Figs. 43b and 44b). In addition, the QY was measured to be 23.4% and 21.6% at a molar ratio of 20% of *R*- or *S*-Cu_6 in BTA/phol/Ag_6/Cu_6 co-assembly systems, corresponding to a 4-fold increase over Cu_6 self-assemblies (5.2% for *R*-Cu_6, 5.0% for *S*-Cu_6) (Supplementary Table 2). The emission lifetime of Ag_6 clusters at 573 nm in the homochiral BTA/*S*-phol/*S*-Ag_6/*S*-Cu_6 co-assembly systems gradually decreased (τ = 9.38 μs → 6.32 μs) as the content of *S*-Cu_6 increased from 0.1% to 3%. However, with the further increase in the amount of Cu_6 clusters from 5% to 20%, the emission lifetime gradually increased (τ = 9.24 μs → 11.01 μs), approaching the lifetime of Cu_6 clusters at 750 nm (Supplementary Fig. 45 and Supplementary Table 13). To further elucidate this phenomenon, ESI-MS was conducted by rapidly mixing Ag_6 and Cu_6 clusters in their DMF solution. The HRMS results showed that the major frag peaks were $[S\text{-}Ag_2Cu_4 + Na]^+$, m/z = 1658.7025, and $[S\text{-}Ag_3Cu_3 + Na]^+$, m/z = 1703.0250, which suggests that *S*-Ag_6 and *S*-Cu_6 immediately exchange metal ions to form *S*-Ag_xCu_{6-x} (x = 1, 2, 3, 4, 5) alloy clusters in DMF solution (Supplementary Figs. 46 and 47). Given the complexity of MS characterization conditions, UV-Vis spectra and ^{1}H NMR spectroscopy were conducted to further confirm the occurrence of rapid kinetic processes in the mixed cluster system (Supplementary Fig. 48). The results confirmed that the addition of Cu_6 clusters to the Ag_6 cluster-based system led to the formation of Ag_xCu_{6-x} alloy clusters. With the increase in the amount of Cu_6 clusters, the emission color of Ag_xCu_{6-x} alloy clusters gradually red-shifted from yellow to near-infrared light (Supplementary Fig. 49). These results demonstrate that the ET process of BTA/phol/Ag_6/Cu_6 co-assembly systems from Ag_6 to Ag_xCu_{6-x} alloy clusters occurred when a tiny amount of Cu_6 clusters was added. As the amount of Cu_6

clusters further increased, the ET process became subtle. More intriguingly, similar to BTA/Ag_6 and BTA/phol/Ag_6 systems, the CPL signals of BTA/phol/Ag_6/Cu_6 quaternary systems were distinctly larger than those of BTA/Ag_6/Cu_6 ternary systems. With the addition of Cu_6 clusters, the CPL peak at 580 nm underwent hypochromatic-shifted and gradually weakened under 330 nm excitation, while the CPL peak at 750 nm gradually enhanced for the BTA/phol/Ag_6/Cu_6 system. When the molar ratio of Cu_6 clusters reached 20%, the $|g_{lum}|$ value at 750 nm reached ~0.05, which is 2.5-fold larger than that of BTA/Ag_6/Cu_6 systems ($|g_{lum}|$ = ~0.02) (Fig. 5f and Supplementary Figs. 42 and 50 and Supplementary Tables 14–17). Overall, the utilization of metal cluster (Ag_6 and Cu_6 clusters) as chiral seeds and Ag_6 clusters as relay baton garnered the relayed chirality-controlled LHSs, improving the g_{lum} and QY of clusters via efficient ET and CPET processes. Furthermore, the g_{lum} of clusters was obviously amplified by the synergistic effect of chiral alcohols, generating a broad CPL emission range from blue to near-infrared light with a high $|g_{lum}|$ value of 0.05.

Multilevel CPL information encryption

Recently, information encryption utilizing multi-color CPL materials has shown great potential in the field of chiraloptics[25]. Metal cluster-based LHSs, which integrate multi-color emission and CPL characteristics, exhibit fantastic encryption features and enable the fabrication of multi-color 3D CPL barcodes. Each barcode consists of four groups of eight bars, corresponding to four sets of standard ASCII characters in binary codes. Upon photoluminescence (PL) and CPL detection, per luminous bar outputs the number "1," while per non-luminous bar outputs the number "0." Under 365 nm UV irradiation, the blue-luminous BTA/*S*-phol bars, cyan-luminous BTA/*S*-phol/*S*-Ag_6-5% bars, orange-luminous BTA/*S*-phol/*S*-Ag_6-20% bars, and red-luminous BTA/*S*-phol/*S*-Ag_6/*S*-Cu_6-20% bars generate CPL signals, wherein the real information is stored in the barcode. Conversely, the luminescent BTA, BTA/rac-Ag_6-5%, and BTA/rac-Ag_6-20% bars do not exhibit CPL signals, and they are camouflaged within the barcode. When observed under 365 nm UV light, per group of eight bars can be directly converted into an ASCII binary code. By referring to the standard ASCII character table, the fake information "Kium" can be obtained due to the presence of the camouflage luminescent codes. When the luminescent barcode is analyzed via CPL detection and converted into ASCII binary code, the real information "Chem" is accurately retrieved (Fig. 6 and Supplementary Figs. 51 and 52). Under 400 nm UV light, irrespective of reading the luminescent barcode directly or via the CPL barcode, the information obtained is incomplete owing to the non-luminescent BTA and BTA/phol. Such metal cluster-controlled chiral LHSs, with multi-color PL and CPL characteristics along with excitation wavelength responses, hold considerable promise for practical applications in advanced information encryption.

Discussion

In this work, chirality-controlled LHSs with high g_{lum} were successfully constructed by chiral metal cluster-driven chirality/ET and the synergistic effect of chiral alcohols. The achiral C_3-symmetric blue-light supramolecular donor, BTA molecules, self-assembled into racemic nanoribbons, which were transformed into helical nanoribbons via chirality transfer mediated by Ag_6 clusters acting as chiral "Sergeant". These helical nanoribbons imparted supramolecular chirality to the Ag_6 clusters through helically oriented arrangement, resulting in strong CPL signals of the Ag_6 clusters with $|g_{lum}|$ of 0.01 via ET and CPET mechanisms. Furthermore, the CPL intensity of the Ag_6 clusters was distinctly amplified in the presence of the synergistic effect of *S*/*R*-phol within homochiral BTA/phol/Ag_6 LHSs, achieving a $|g_{lum}|$ value of 0.06, which is 30-fold larger than that of the self-assembled Ag_6 clusters. Building on these findings, to further broaden the CPL emission range, the Cu_6 clusters with near-infrared light are incorporated into the homochiral BTA/phol/Ag_6 LHSs. In this hierarchical assembly, the Ag_6 clusters functioned as a relay baton, facilitating the formation of Ag_xCu_{6-x} alloy clusters with broad CPL emission. This enabled continuous chirality and ET transfers from the BTA assemblies to Ag_6 clusters and then to Ag_xCu_{6-x} alloy clusters, culminating in optimal near-infrared CPL emission with $|g_{lum}|$ of 0.05 and QY of 23%. This work establishes a universal strategy for designing chirality-controlled LHSs with high g_{lum} and broad CPL emission from blue to near-infrared region, provides valuable insights into continuous chirality transfer and amplification and synergistic chirality in metal cluster-based LHSs,

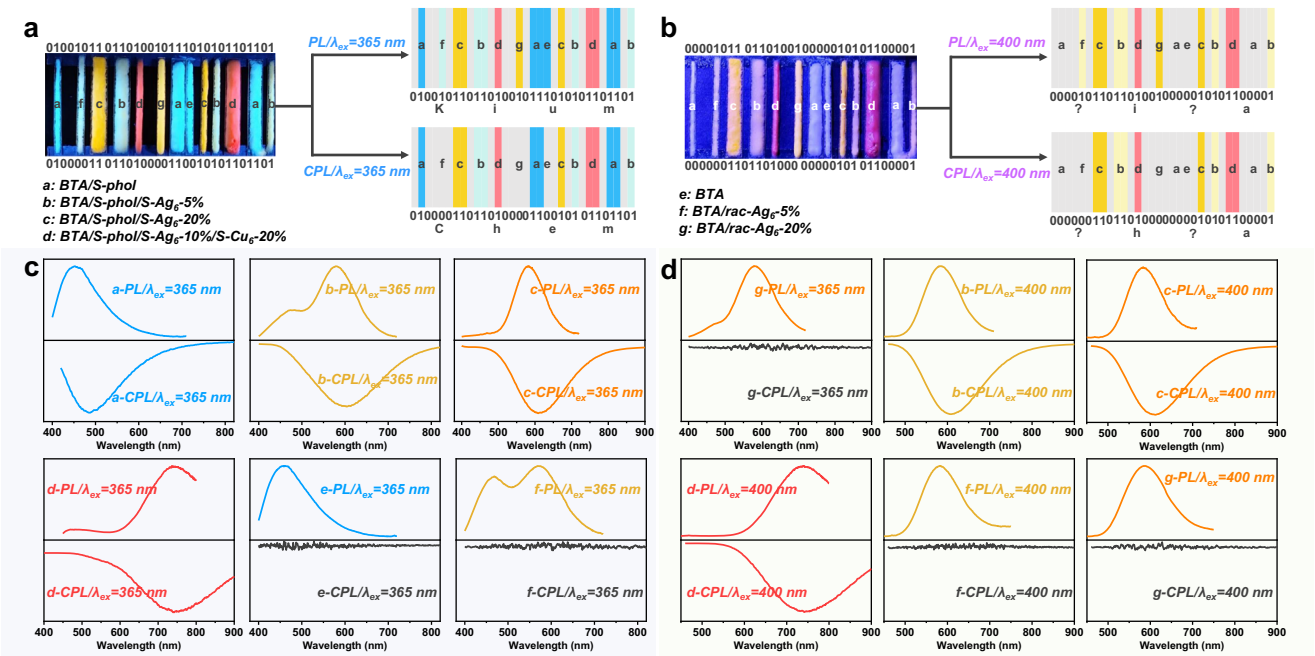

Fig. 6 | Potential application of CPL information encryption through a 3D barcode with tunable PL and CPL in BTA/phol/Ag_6/Ag_xCu_{6-x} LHSs. **a**, **b** Schematic showing a barcode with standard ASCII characters and encrypted PL and CPL with different wavelengths of UV light (λ_{ex} = 365 nm/400 nm) for information encryption. **c**, **d** Normalized PL and CPL spectra of the bars (a–g) with different wavelengths of UV light (λ_{ex} = 365 nm/400 nm).

and develops a promising application in CPL-based information encryption.

Methods

Synthesis of *R*/*S*-Ag_6

R-Ag_6 and *S*-Ag_6 were synthesized according to the literature procedure[62]. Specifically, *R*-ligand or *S*-ligand (*D*/*L*-4-phenylthiazolidine-2-thione) (19.5 mg, 0.1 mmol) and $AgNO_3$ (16.9 mg, 0.1 mmol) were dissolved in a mixture of DMAc/CH_3CN (4 mL, 3/1, v/v) solution. After stirring for 10 min at room temperature, a clear yellow solution was obtained and then kept in the dark for 2–3 days to get light yellow block crystals of *R*-Ag_6 or *S*-Ag_6. Yield: 69.3% for *S*-Ag_6 based on Ag.

Synthesis of *R*/*S*-Cu_6

R-Cu_6 and *S*-Cu_6 were synthesized following the literature methold[65]. CuI (19.0 mg, 0.1 mmol) was dissolved in CH_3CN (2 mL) solution, and the *R*-ligand and *S*-ligand (19.5 mg, 0.1 mmol) dissolved in 6 mL DMF were added to the above solution. After stirring for 15 min at room temperature, a clear yellow solution was obtained and then slowly volatilized in the dark for approximately 10 days to get red block crystals *R*-Cu_6 and *S*-Cu_6. Yield: 49.8% for *S*-Cu_6 based on Cu.

Preparation of the gel for BTA self-assembly

BTA (6 mg, 10.6 mmol) was dissolved in DMF (0.6 mL) in a 2 mL microtube, and then deionized water (0.4 mL) was added to the solution. The mixture was shaken until homogeneous and aged by heating in a water bath at 60 °C for 90 min, yielding a white gel.

Preparation of the gels for BTA/phol co-assemblies

BTA (6 mg, 10.6 mmol) was dissolved in DMF (0.6 mL) in a 2 mL microtube. Then, *S*/*R*-phol (0.07 mL) was added, followed by the addition of deionized water (0.4 mL). The mixture was shaken until homogeneous, which was aged by heating in a water bath at 60 °C for 90 min, yielding a white gel.

Preparation of the gels for BTA/Ag_6 co-assemblies

BTA (6 mg, 10.6 mmol) and *R*/*S*-Ag_6 (molar ratios ranging from 0.1% to 20%) were dissolved in DMF (0.6 mL) in a 2 mL microtube, and then deionized water (0.4 mL) was added to the solution. The mixture was shaken until homogeneous, which was aged by heating in a water bath at 60 °C for 90 min, yielding a yellow gel.

Preparation of the gels for BTA/phol/Ag_6 co-assemblies

BTA (6 mg, 10.6 mmol) and *R*/*S*-Ag_6 (molar ratios ranging from 0.1% to 20%) were dissolved in DMF (0.6 mL) in a 2 mL microtube. Then, *R*/*S*-phol (0.07 mL) was added, followed by the addition of deionized water (0.4 mL). The mixture was shaken until homogeneous, which was aged by heating in a water bath at 60 °C for 90 min, yielding a yellow gel.

Preparation of CD/CPL films for BTA, BTA/phol, BTA/Ag_6, BTA/phol/Ag_6 assemblies

A volume of 0.10 mL of BTA (or BTA/phol, BTA/Ag_6, BTA/phol/Ag_6) gel was taken and applied by dropping onto a 2 × 2 cm quartz slice and air-dried for 2 h, obtaining a dry film.

Preparation of SEM/TEM samples for BTA, BTA/phol, BTA/Ag_6, BTA/phol/Ag_6, Ag_6 assemblies

A volume of 1.8 µL of BTA (or BTA/phol, BTA/Ag_6, BTA/phol/Ag_6) gel was taken and applied by dropping onto a clean silicon chip (carrier mesh). After the samples dried at room temperature overnight, their morphologies were characterized by SEM and TEM instruments.

Data availability

All data are available from S.Q.Z. or Y.X.Y. upon request. The data generated in this study are provided in the Supplementary Information/Source data file. The X-ray crystallographic coordinates for structures reported in this study have been deposited at the Cambridge Crystallographic Data Centre (CCDC), under deposition numbers CCDC 2394282 (*R*-Cu_6) and 2394819 (*S*-Cu_6). These data can be obtained free of charge from The Cambridge Crystallographic Data Centre via www.ccdc.cam.ac.uk/data_request/cif. Source data are provided with this paper.

References

1. Karsenti, E. & Vernos, I. The mitotic spindle: a self-made machine. *Science* **294**, 543–547 (2001).
2. Wegst, U., Bai, H., Saiz, E., Tomsia, A. & Ritchie, R. Bioinspired structural materials. *Nat. Mater.* **14**, 23–36 (2015).
3. Yano, K. et al. Nematic-to-columnar mesophase transition by in situ supramolecular polymerization. *Science* **363**, 161–165 (2019).
4. Tan, J. et al. Structural basis of assembly and torque transmission of the bacterial flagellar motor. *Cell* **184**, 2665–2679 (2021).
5. Nepal, D. et al. Hierarchically structured bioinspired nanocomposites. *Nat. Mater.* **22**, 18–35 (2023).
6. Morrow, S., Bissette, A. & Fletcher, S. Transmission of chirality through space and across length scales. *Nat. Nanotechnol.* **12**, 410–419 (2017).
7. Huang, S., Yu, H. & Li, Q. Supramolecular chirality transfer toward chiral aggregation: asymmetric hierarchical self-assembly. *Adv. Sci.* **8**, 2002132 (2021).
8. Nizar, N. S. S. et al. Emergent chiroptical properties in supramolecular and plasmonic assemblies. *Chem. Soc. Rev.* **50**, 11208–11226 (2021).
9. Liao, R., Wang, F., Guo, Y., Han, Y. & Wang, F. Chirality-controlled supramolecular donor-acceptor copolymerization with distinct energy transfer efficiency. *J. Am. Chem. Soc.* **144**, 9775–9784 (2022).
10. Prins, L., Timmerman, P. & David, N. R. Amplification of chirality: the "Sergeants and Soldiers" principle applied to dynamic hydrogen-bonded assemblies. *J. Am. Chem. Soc.* **123**, 10153–10163 (2001).
11. Ikai, T. et al. Control of one-handed helicity in polyacetylenes: Impact of an extremely small amount of chiral substituents. *J. Am. Chem. Soc.* **145**, 24862–24876 (2023).
12. Hall, L. A., D'Alessandro, D. M. & Lakhwani, G. Chiral metal-organic frameworks for photonics. *Chem. Soc. Rev.* **52**, 3567–3590 (2023).
13. Zhang, M. et al. Processable circularly polarized luminescence material enables flexible stereoscopic 3D imaging. *Sci. Adv.* **9**, eadi9944Y (2023).
14. Chen, Y. et al. Enantioselective self-assembly of a homochiral tetrahedral cage comprising only achiral precursors. *Angew. Chem. Int. Ed.* **63**, e202400467 (2024).
15. Huang, J.-H., Dong, X.-Y., Wang, Y.-J. & Zang, S.-Q. Generation and manipulation of chiroptical activities in coinage-metal clusters. *Coord. Chem. Res.* **470**, 214729 (2022).
16. Song, Q. et al. Efficient artificial light-harvesting system based on supramolecular peptide nanotubes in water. *J. Am. Chem. Soc.* **143**, 382–389 (2021).
17. Chen, D., Xiao, T., Monflier, É & Wang, L. Multi-step FRET systems based on discrete supramolecular assemblies. *Commun. Chem.* **7**, 88 (2024).
18. Wu, Y., Wang, Y., Yu, X. & Song, Q. Comprehensive study of artificial light-harvesting systems with a multi-step sequential energy transfer mechanism. *Adv. Sci.* **11**, 2404269 (2024).
19. Sarkar, A., Dhiman, S., Chalishazar, A. & George, S. J. Visualization of stereoselective supramolecular polymers by chirality-controlled energy transfer. *Angew. Chem. Int. Ed.* **56**, 13767–13771 (2017).
20. Sethy, R. et al. Enantioselective light harvesting with perylenediimide guests on self-assembled chiral naphthalenediimide nanofibers. *Angew. Chem. Int. Ed.* **56**, 15053–15057 (2017).

21. Cao, S. et al. Photoactivated nanomotors via aggregation induced emission for enhanced phototherapy. *Nat. Commun.* **12**, 2077 (2021).
22. Delor, M. et al. Exploiting chromophore-protein interactions through linker engineering to tune photoinduced dynamics in a biomimetic light-harvesting platform. *J. Am. Chem. Soc.* **140**, 6278–6287 (2018).
23. Jing, Y.-N., Li, S.-S., Su, M., Bao, H. & Wan, W.-M. Barbier hyperbranching polymerization-induced emission toward facile fabrication of white light-emitting diode and light-harvesting film. *J. Am. Chem. Soc.* **141**, 16839–16848 (2019).
24. Li, W.-J. et al. Artificial light-harvesting systems based on AIEgen-branched rotaxane dendrimers for efficient photocatalysis. *Angew. Chem. Int. Ed.* **60**, 18761–18768 (2021).
25. Xu, X.-Q. et al. Chiral rotaxane-branched dendrimers as relays in artificial light-harvesting systems with boosted circularly polarized luminescence. *Angew. Chem. Int. Ed.* **64**, e202419434 (2025).
26. Yuan, Y.-X., Zhang, J.-N., Wang, J.-R., Li, K. & Zang, S.-Q. Chiral silver cluster-based light-harvesting systems: enantioselective chirality transfer and amplified circularly polarized luminescence. *Chem* **10**, 1766–1782 (2024).
27. Ji, L. et al. Cooperative chirality and sequential energy transfer in a supramolecular light-harvesting nanotube. *Angew. Chem. Int. Ed.* **58**, 844–848 (2019).
28. Yuan, Y.-X. et al. Fluorescent TPE macrocycle relayed light-harvesting system for bright customized-color circularly polarized luminescence. *J. Am. Chem. Soc.* **144**, 5389–5399 (2022).
29. Wu, Y. et al. Circularly polarized fluorescence resonance energy transfer (C-FRET) for efficient chirality transmission within an intermolecular system. *Angew. Chem. Int. Ed.* **60**, 24549–24557 (2021).
30. Yang, D. et al. Steering triplet-triplet annihilation upconversion through enantioselective self-assembly in a supramolecular gel. *J. Am. Chem. Soc.* **143**, 13259–13265 (2021).
31. Yao, L. et al. Metallophilic interaction-mediated hierarchical assembly and temporal-controlled dynamic chirality inversion of metal-organic supramolecular polymers. *ACS Nano* **17**, 2159–2169 (2023).
32. Yang, Y.-H., He, R., Qin, Y. & Zhang, L. Metal-ion-triggered symmetry breaking of completely achiral azobenzene amphiphiles in water. *Nanoscale* **16**, 9075–9083 (2024).
33. Wang, X., Ma, S., Zhao, B. & Deng, J. Frontiers in circularly polarized phosphorescent materials. *Adv. Funct. Mater.* **33**, 2214364 (2023).
34. Yuan, Y.-X. et al. The largest CPL enhancement by further assembly of self-assembled superhelices based on the helical TPE macrocycle. *Mater. Horiz.* **7**, 3209–3216 (2020).
35. Yang, K., Ma, S., Wu, Y., Zhao, B. & Deng, J. Circularly polarized fluorescence energy transfer for constructing multicolor circularly polarized luminescence films with controllable handedness. *Chem. Mater.* **35**, 1273–1282 (2023).
36. Chen, H., Gu, Z.-G. & Zhang, J. Chiral-induced ultrathin covalent organic frameworks nanosheets with tunable circularly polarized luminescence. *J. Am. Chem. Soc.* **144**, 7245–7252 (2022).
37. Yuan, Y.-X. et al. Circularly polarized luminescence and SHG chiral signals of helical TPE macrocycles. *Chin. J. Chem.* **39**, 3353–3359 (2021).
38. Yang, S., Zhang, S., Hu, F., Han, J. & Li, F. Circularly polarized luminescence polymers: From design to applications. *Coord. Chem. Rev.* **485**, 215116 (2023).
39. Han, H., He, Y., Wang, D., Han, T. & Tang, B. Z. Aggregation-induced emission polymer systems with circularly polarized luminescence. *Aggregate* **4**, e331 (2023).
40. Zhou, Y. et al. Helical-caging enables single-emitted large asymmetric full-color circularly polarized luminescence. *Nat. Commun.* **15**, 251 (2024).
41. Ikai, T., Okubo, M. & Wada, Y. Y. Helical assemblies of one-dimensional supramolecular polymers composed of helical macromolecules: Generation of circularly polarized light using an infinitesimal chiral source. *J. Am. Chem. Soc.* **142**, 3254–3261 (2020).
42. Park, G. et al. Enhancing circularly polarized phosphorescence via integrated top-down and bottom-up approach. *Angew. Chem. Int. Ed.* **62**, e202309762 (2023).
43. Gong, Z.-L. et al. Boost the circularly polarized phosphorescence of chiral organometallic platinum complexes by hierarchical assembly into fibrillar networks. *Angew. Chem. Int. Ed.* **63**, e202402882 (2024).
44. Xu, M. et al. Designing hybrid chiral photonic films with circularly polarized room-temperature phosphorescence. *ACS Nano* **14**, 11130–11139 (2020).
45. Zhang, D. et al. On-demand circularly polarized room-temperature phosphorescence in chiral nematic nanoporous silica films. *Adv. Opt. Mater.* **10**, 2102015 (2022).
46. Zhao, B., Kai, P. & Deng, J. Combining chiral helical polymer with achiral luminophores for generating full-color, on-off, and switchable circularly polarized luminescence. *Macromolecules* **52**, 376–384 (2019).
47. Zhao, B., Yu, H., Kai, P., Tan, Z. & Deng, J. Multifarious chiral nanoarchitectures serving as handed-selective fluorescence filters for generating full-color circularly polarized luminescence. *ACS Nano* **14**, 3208–3218 (2020).
48. Zhong, H., Gao, X., Zhao, B. & Deng, J. "Matching Rule" for generation, modulation and amplification of circularly polarized luminescence. *Acc. Chem. Res.* **57**, 1188–1201 (2024).
49. Zhang, G. et al. Precise Modulation of circularly polarized luminescence via polymer chiral co-assembly and contactless dynamic chiral communication. *Angew. Chem. Int. Ed.* **63**, e202401077 (2024).
50. Wang, X. et al. Constructing diverse switchable circularly polarized luminescence via a single azobenzene polymer film. *Chin. Chem. Lett.* **36**, 110047 (2025).
51. Zhang, G. & Zhang, W. New concept on the generation and regulation of circularly polarized luminescence. *Chem. Eur. J.* **31**, e202404020 (2025).
52. Chen, S. H. et al. Circularly polarized light generated by photoexcitation of luminophores in glassy liquid-crystal films. *Nature* **397**, 506–508 (1999).
53. Yang, Y., da Costa, R. C., Fuchter, M. J. & Campbell, A. J. Circularly polarized light detection by a chiral organic semiconductor transistor. *Nat. Photonics* **7**, 634–638 (2013).
54. Song, I. et al. Helical polymers for dissymmetric circularly polarized light imaging. *Nature* **617**, 92–99 (2023).
55. MacKenzie, L. E. & Pal, R. Circularly polarized lanthanide luminescence for advanced security inks. *Nat. Chem. Rev.* **5**, 109–124 (2021).
56. Guo, Q. et al. Multimodal-responsive circularly polarized luminescence security materials. *J. Am. Chem. Soc.* **145**, 4246–4253 (2023).
57. Lin, S. et al. Photo-triggered full-color circularly polarized luminescence based on photonic capsules for multilevel information encryption. *Nat. Commun.* **14**, 3005 (2023).
58. Lu, G. et al. Semitransparent circularly polarized phosphorescent organic light-emitting diodes with external quantum efficiency over 30% and dissymmetry factor close to 10^{-2}. *Adv. Funct. Mater.* **31**, 2102898 (2021).
59. Zhang, D.-W., Li, M. & Chen, C.-F. Recent advances in circularly polarized electroluminescence based on organic light-emitting diodes. *Chem. Soc. Rev.* **49**, 1331–1343 (2020).
60. Zhong, X.-S. et al. Circularly polarized organic light-emitting diodes based on chiral hole transport enantiomers. *Adv. Mater.* **36**, 2311857 (2024).

61. Furlan, F. et al. Chiral materials and mechanisms for circularly polarized light-emitting diodes. *Nat. Photonics* **18**, 658–668 (2024).
62. Han, Z. et al. Ultrastable atomically precise chiral silver clusters with more than 95% quantum efficiency. *Sci. Adv.* **6**, eaay0107 (2020).
63. Ma, X.-H. et al. High-efficiency pure blue circularly polarized phosphorescence from chiral N-heterocyclic-carbene-stabilized copper(I) clusters. *J. Am. Chem. Soc.* **145**, 25874–25886 (2023).
64. Kumar, J. & Nakashima, T. Amplifying circularly polarized luminescence in chirality-matched dye-silver clusters. *Chem* **10**, 1628–1630 (2024).
65. Han, Z. et al. Smart reversible transformations between chiral superstructures of copper clusters for optical and chiroptical switching. *J. Am. Chem. Soc.* **145**, 6166–6176 (2023).
66. Zhang, C., Si, W.-D., Wang, Z., Tung, C.-H. & Sun, D. Chiral ligand-concentration mediating asymmetric transformations of silver nanoclusters: NIR-II circularly polarized phosphorescence lighting. *Angew. Chem. Int. Ed.* **63**, e202404545 (2024).
67. Xiao, C., Li, C., Huang, K., Duan, P. & Wang, Y. Cascade energy transfer boosted near-infrared circularly polarized luminescence of nanofibers from an exclusively achiral system. *Nanoscale* **15**, 10820–10825 (2023).
68. Li, C., Huang, K., Xiao, C., Shi, Y. & Duan, P. Controlling assembly-induced symmetry-breaking by tuning the vortex-responsive nanostructures. *Nano Res.* **16**, 13450–13456 (2023).
69. Shen, Z. et al. Asymmetric catalysis mediated by a mirror symmetry-broken helical nanoribbon. *Nat. Commun.* **10**, 3976 (2019).
70. Sang, Y., Yang, D., Shen, Z., Duan, P. & Liu, M. Mechanically controlled and consecutively boosted circularly polarized luminescence of nanoassemblies from achiral molecules. *J. Phys. Chem. C* **124**, 17274–17281 (2020).
71. Zhou, M. et al. Steering nanohelix and upconverted circularly polarized luminescence by using completely achiral components. *ACS Nano* **15**, 2753–2761 (2021).
72. Panahi-Sarmad, M. et al. Liquid printing in nanochitin suspensions: interfacial nanoparticle assembly toward volumetric elements, organic electronics and core-shell filaments. *Small Methods* **9**, 2500100 (2025).
73. Smilgies, D.-M. Scherrer grain-size analysis adapted to grazing-incidence scattering with area detectors. *J. Appl. Cryst.* **42**, 1030–1034 (2009).
74. Xiao, Y. & Lu, X. Morphology of organic photovoltaic non-fullerene acceptors investigated by grazing incidence X-ray scattering techniques. *Mater. Today Nano* **5**, 100030 (2019).
75. Kao, K.-C., Lin, C.-H., Chen, T.-Y., Liu, Y.-H. & Mou, C.-Y. A general method for growing large area mesoporous silica thin films on flat substrates with perpendicular nanochannels. *J. Am. Chem. Soc.* **137**, 3779–3782 (2015).
76. Hu, M. et al. Tunable circularly polarized luminescence from single crystal and powder of the simplest tetraphenylethylene helicate. *ACS Nano* **15**, 16673–16682 (2021).
77. Khorloo, M. et al. Enantiomeric switching of the circularly polarized luminescence processes in a hierarchical biomimetic system by film tilting. *ACS Nano* **15**, 1397–1406 (2021).

Acknowledgements

This work was supported by the National Natural Science Foundation of China (92356304, S.Q.Z.; 92061201, S.Q.Z.; 22475195, Y.X.Y.; and 22101263, Y.X.Y.), Postdoctoral Science Foundation of China (No. 2024M762981, Y.X.Y.), National Key R&D Program of China (2021YFA1200300, S.Q.Z.), and Zhengzhou University.

Author contributions

S.Q.Z., Y.X.Y. and J.Y.W. conceived and designed the experiments. T.L.G., J.R.W., Z.H. and Y.X.Y. conducted the synthesis and characterization. T.L.G., J.R.W. and Z.H. drew pictures in the manuscript. S.Q.Z., Y.X.Y. and T.L.G. analyzed the experimental results. S.Q.Z., Y.X.Y. and J.Y.W. helped to revise the writings. T.L.G., Y.X.Y. and S.Q.Z. co-wrote the manuscript.

Competing interests

The authors declare no competing interests.

Additional information

Supplementary information The online version contains supplementary material available at https://doi.org/10.1038/s41467-025-64638-x.

Correspondence and requests for materials should be addressed to Jia-Yin Wang, Ying-Xue Yuan or Shuang-Quan Zang.

Peer review information *Nature Communications* thanks Ahmadreza Ghaffarkhah and the other, anonymous, reviewers for their contribution to the peer review of this work. A peer review file is available.